AIAA JOURNAL
Vol. 58, No. 11, November 2020



# Numerical Investigation of an Actively and Passively Controlled Skeleton-Reinforced Caudal Fin

Guangyu Shi* and Qing Xiao†
*University of Strathclyde, Glasgow, Scotland G4 0LZ, United Kingdom*
and
Qiang Zhu‡
*University of California, San Diego, La Jolla, California 92093*

https://doi.org/10.2514/1.J059141

**We numerically investigate the propulsion performance of a skeleton-reinforced caudal fin with both active and passive control mechanisms. In our fluid–structure interaction model, the embedded rays are depicted as nonlinear beams while the flow is simulated using a Navier–Stokes solver. Kinematically, the fin is activated by a sway motion at the basal ends of the rays and distributed time-varying forces along each ray individually. The dynamics of the fin is closely associated with the exact distribution of phase lags (between the sway motion and external forces) among the rays. We find that the fin's performance can be significantly enhanced by active control when the mean phase lag is less than 90 deg. Among different deformation patterns, the cupping deformation (*C* mode) produces the best propulsion performance and the W-shape deformations (*W* mode) have a similar (yet less pronounced) effect. Asymmetric deformations such as the heterocercal mode (*H* mode) and undulation mode (*S* mode) are able to generate vertical forces. Compared with the *H* mode, the *S* mode creates less thrust force, but it significantly reduces the transverse force, making it more suitable in cases when there is no other mechanism to balance this transverse force (for example, during the braking maneuver).**



## Nomenclature

| | | |
|---|---|---|
| $A_{p,i}$ | = | amplitude of induced yaw motion of $i$th ray |
| $a$ | = | speed of sound |
| $C_P$ | = | instantaneous power expenditure coefficient |
| $C_{\text{pre}}$ | = | pressure coefficient |
| $C_T$ | = | instantaneous thrust coefficient |
| $C_Y$ | = | instantaneous lateral force coefficient |
| $C_Z$ | = | instantaneous vertical force coefficient |
| $\overline{C}_P$ | = | time-averaged power expenditure coefficient |
| $\overline{C}_T$ | = | time-averaged thrust coefficient |
| $\overline{C}_Z$ | = | time-averaged vertical force coefficient |
| $c$ | = | length of the fin |
| $dt$ | = | physical time step |
| $F_i$ | = | time-varying distributed force acting on $i$th ray |
| $F_0$ | = | magnitude of time-varying distributed force |
| $h$ | = | thickness of the fin |
| $I$ | = | second inertia moment of the ray |
| $K_b$ | = | mean normalized bending stiffness of all rays |
| $K_i$ | = | normalized bending stiffness of $i$th ray |
| $M_a$ | = | local flow Mach number, defined as $U/a$ |
| $M_{a,\infty}$ | = | freestream flow Mach number |
| $\overline{m}_i$ | = | mass ratio of $i$th ray |
| $N$ | = | number of rays |
| $Re$ | = | Reynolds number |
| $S_{t,a}$ | = | Strouhal number based on leading-edge amplitude |
| $T$ | = | sway motion period of the fin |
| $U_\infty$ | = | freestream flow velocity |
| $y(t)$ | = | sway motion of the fin's leading edge |
| $y_P$ | = | induced yaw motion of the ray |
| $y_0$ | = | sway motion amplitude of the fin's leading edge |
| $\eta$ | = | propulsion efficiency |
| $\rho$ | = | fluid density |
| $\rho_{s,i}$ | = | structural density of $i$th ray |
| $\varphi_{\text{diff}}$ | = | phase difference between the maximum and minimum values of $\varphi_i$ |
| $\varphi_i$ | = | phase lag between sway motion and actuation force of $i$th ray |
| $\varphi_{\text{mean}}$ | = | mean value of phase lags among the rays |
| $\psi_i$ | = | phase lag between sway motion and the induced yaw motion of $i$th ray |
| $\omega$ | = | motion frequency |

Received 19 October 2019; revision received 10 February 2020; accepted for publication 22 May 2020; published online 30 September 2020. 

*Ph.D. Student, Department of Naval Architecture, Ocean and Marine Engineering.
†Reader, Department of Naval Architecture, Ocean and Marine Engineering; qing.xiao@strath.ac.uk. Senior Member AIAA (Corresponding Author).
‡Professor, Department of Structural Engineering.

## I. Introduction

CAUDAL fins, which are traditionally modeled as rigid or elastic flapping foils [1–3], play an important role in fish locomotion. Those simplified caudal fin models usually possess only two-degree-of-freedom motions (e.g., sway and yaw). In comparison, the caudal fin of a real fish is characterized by a much more complicated composite structure, including a collagenous membrane, bony rays, and intrinsic musculature. Structurally, a caudal fin forms a ray-strengthened membrane system, where the Young's modulus of the membrane is much smaller than that of the supporting rays. Therefore, the stiffness of the fin is mainly determined by those embedded rays. The nonuniform flexibility of each ray and the differences among the rigidities of different rays impart an anisotropic structural property of the fin so that it may undergo (presumably) beneficial passive deformations under hydrodynamic loads. This passive flow control strategy is believed to improve the propulsion efficiency, enhance the thrust generation, and reduce the lateral forces [4,5]. The benefits of anisotropic material property can also be seen from a two-dimensional study of a pectoral fin [6], where the performance of the pectoral fin can be significantly improved with a strengthened leading edge.

In addition to the aforementioned passive control mechanism enabled by the anisotropic material property, fish fins also possess two other important features that enable active control over their deformations. First, each fin ray can be actuated individually through the sophisticated musculature system. Besides, each ray has by itself a remarkable biomechanical system for motion actuation. According to previous morphological studies [7,8], a fin ray is composed of a

central cartilage pad surrounded by paired, segmented bony elements called hemitrichs, which are connected with short ligaments and elastic fibers (tendons) at the ends. The basal end of each ray is attached to four separate muscles. By pulling the tendons, one hemitrich can slide past the other one, creating a distributed bending moment along the length of a ray [7]. Through the embedded tendons and the unique bilaminar design of the ray, a fish is able to actively modify the curvature of the ray and change the bending stiffness of the ray itself. As observed in previous experiments with live bluegill sunfish (*Lepomis macrochirus*), the fish can actively modulate their caudal fin shapes to accomplish different swimming behaviors; e.g., *C* mode and *W* mode are usually used for steady swimming, whereas the *S* mode is observed in the braking maneuver [9]. These deformation patterns are fully three-dimensional; thus, they cannot be achieved by flapping foils with simple flexibility.

Recently, bioinspired caudal fins have attracted increasing attention from scientists. Esposito et al. [10] constructed and tested a sophisticated robotic fin by imitating the caudal fin of bluegill sunfish. With six independently controlled and actuated rays, this robotic fin was able to produce some motions (e.g., *C* mode, *W* mode, and *S* mode) observed in a live fish experiment. They found that the cupping motion was able to create the largest thrust in most cases, whereas the undulation motion produced lift of the same magnitude as thrust. Experimentally, Lucas et al. [11] examined four fishlike foil models: two with uniform stiffness and the others with stiffer anterior regions and softer posterior regions. The fishlike foils with nonuniform chordwise stiffness had enhanced performance when compared with those with uniform flexibility. This finding is reminiscent of a numerical study where the propulsion performance of a pectoral fin was improved by a strengthened leading edge [6].

In addition to experiments, some researchers are dedicated to establishing computational models to investigate the fluid–structure interactions of biomimetic caudal fins. Zhu and Shoele [4] established a fluid–structure interaction model to study the performance of a ray-supported caudal fin. With the individual rotation of each ray at the basal end, the fin was able to achieve both homocercal and heterocercal deformations. They concluded that, in both cases, the flexibility can enhance the propulsion performance due to the introduction of an effective yaw motion and reduction of lateral forces. Similarly, Zhu and Bi [12] examined the effect of various spanwise deformations on the thrust generation of a caudal fin. Different deformation patterns were accomplished passively via specific bending stiffness distributions among the supporting rays. They found that compared with a fin with uniform distribution of ray stiffness, a fin with nonuniformly distributed ray stiffness (but the same averaged value) can achieve further performance improvement. However, in their model, a boundary-element method based on potential flow theory was used for the fluid dynamics, where the leading-edge vortices and the vortices shed from the dorsal and ventral edges were not considered. More recently, Shi et al. [13] developed a fluid–structure interaction solver by coupling a Navier–Stokes flow solver with a nonlinear beam model. It was then applied to investigate the propulsion performance of a three-dimensional ray-strengthened caudal fin with various spanwise ray stiffness distributions. They found that certain deformation patterns observed in the experiment could be reproduced by specific ray stiffness distributions; among which, the cupping distribution required the least power input, whereas the uniform distribution performed the best in terms of thrust generation. Incidentally, the uniform stiffness distribution also caused a *C* mode with relatively smaller phase differences between different rays. The *H* mode, on the other hand, yielded considerable vertical force, which may play an important role in fish maneuvers.

In spite of the efforts to understand the control mechanisms of fish locomotion, most studies of bioinspired finlike devices only considered the anisotropic flexibility and/or individual activation of rays. As mentioned earlier, ray-finned fish are capable of actively changing the curvature and stiffness of the rays. However, this important feature, with a few exceptions [7,14], has not been accounted for in existing studies.

In the present paper, we numerically investigate the propulsion performance and shape modulation of a simplified caudal fin model. Unlike previous work by Shi et al. [13], which was focused on passive fin deformation only, hereby we engage in a much broader scope in which both active and passive shape control mechanisms are included. Moreover, via in-depth study of the fin motion and the near-body flowfield, we provide a physical explanation of the performance enhancement through carefully controlled deformations.

In this model, the fin rays are represented by nonlinear Euler–Bernoulli beams, whereas the flow around the caudal fin is resolved by solving the unsteady Navier–Stokes equations with a finite volume approach. The rays are activated by two means: 1) a single sinusoidal sway motion imposed at their basal ends, mimicking the motion of the posterior part of the fish; and 2) an independent activation load uniformly distributed along each ray, imitating the pulling effect of the tendons. Subsequently, the fin is deformed both actively and passively under the effects of the activation load, the inertia, the elasticity, the hydrodynamic force, and the constraint from the soft membrane.

Our current study is inspired by the fact that ray-finned fish are capable of actively changing the curvature of the fin rays so as to modulate their fin shapes. We are also motivated by the scientific need to understand the fundamental mechanisms in fish locomotion as well as the practical applications of these biomimetic devices on unmanned underwater vehicles. The present work will be the first systematic numerical investigation on a finlike propeller that considers both the viscous fluid–structure interaction and active curvature control of the fin rays. The objectives are 1) to elucidate the effect of active curvature control on the dynamics and performance of a biomimetic caudal fin; and 2) to identify the key features of the ray-supported fins that enhance their locomotion performance. To isolate the effects of certain characters, it will be more convenient to establish a simplified model rather than exactly copying from nature. From the perspective of biomimetics, it is also preferable to design simple and easily manufactured devices that capture the essential characteristics of fish fins. Therefore, an idealized caudal fin model instead of exact duplications of real fish fins is employed in the present paper. For simplicity, the rotational motions at the basal ends of the rays are not considered.

The rest of this paper is organized as follows: in Sec. II, the geometry, material property, kinematics, and actuation of the simplified caudal fin are described and the parameters characterizing the performance are defined. In the following section, the governing equations and numerical algorithms used in the present fluid–structure interaction solver are briefly reviewed (details are included in a previous publication by Shi et al. [13]). In Sec. IV, the numerical results (including fin deformation, force generation, near-body flowfield, and the underlying mechanism for performance enhancement) are presented. The conclusions are drawn in the final section.

## II. Problem Description

In the present study, the real ray-strengthened caudal fin (Fig. 1a) is geometrically and structurally simplified as a square-shaped membrane supported by $N$ evenly distributed rays (Fig. 1b). This fin has length $c$ in both chordwise and spanwise directions. The thickness of the fin is chosen to be $h = 0.004c$. Each ray is structurally represented by a nonlinear Euler–Bernoulli beam with a uniform Young's modulus. The dimensionless bending stiffness for the $i$th ray is defined as $K_i = E_i I/\rho U_\infty^2 c^3 \quad (i = 1, \ldots, N)$, where $N = 11$, $E_i$ is the Young's modulus of the $i$th ray, $I$ is the second moment of inertia, $\rho$ is the fluid density, and $U_\infty$ is the incoming flow velocity. The mass ratio is defined as $\bar{m}_i = \rho_{s,i} h/\rho c$, where $\rho_{s,i}$ is the density of the $i$ th ray. In the present work, two different spanwise bending stiffness distributions of the ray are studied: 1) uniform stiffness distribution $K_i = K_b$; and 2) cupping stiffness distribution $K_i = K_b \Theta_i/\Theta$, where

$$\Theta_i = 1 + \gamma\left[1 - \sin\left(\frac{\pi(i-1)}{N-1}\right)\right]$$

Here, $K_b$ is the mean dimensionless bending stiffness of all the rays and

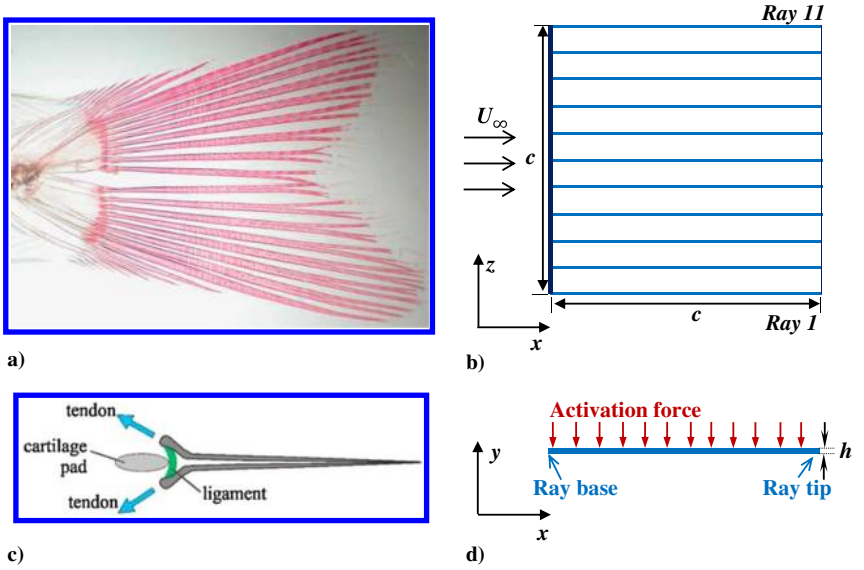


**Fig. 1 Representations of a) caudal fin anatomy of bluegill sunfish (Lepomis macrochirus) [8] and b) idealized rectangular ray-supported caudal fin model. Dorsal views of c) a fin ray with two hemitrichs [7]; and d) present ray model.**

$$\Theta = \frac{1}{N}\sum_{i=1}^{N}\Theta_i$$

The parameter $\gamma$ is selected to be one. The mean value of the stiffness is selected to be $K_b = 3.0$, and the mass ratios of the ray are chosen as $\overline{m}_i = 0.2$. The two different stiffness distributions are depicted in Fig. 2a.

Additionally, we assume that the bending stiffness of the membrane can be neglected; i.e., it can only sustain stretching/compression but not bending. Thus, the constraints provided by the membrane are modeled as distributed linear springs between neighboring rays. Based on numerical tests, we choose the spring constant to be $0.02\rho U_\infty^2 c$, so that the springs are sufficiently flexible to allow large spanwise deformation and yet stiff enough to prevent excessive expansion of the membrane.

Kinematically, the basal ends of all the rays share the same sinusoidal sway motion in the $y$ direction, which imitates the motion of the posterior part of the fish and is expressed as $y(t) = y_0\cos(\omega t)$, where $y_0$ is the sway amplitude and $\omega$ is the motion frequency. The Strouhal number based on the sway amplitude is defined as $S_{t,a} = \omega y_0/\pi U_\infty$. Here, we choose $S_{t,a} = 0.4$. Besides, each ray is also actuated by independent external forces $F_i$ $(i = 1,\ldots,N)$, mimicking the pulling effect of the tendons at the basal end of the ray (see Figs. 1c and 1d). The external loads vary with time as $F_i(t) = F_0\cos(\omega t - \varphi_i)$, where $\varphi_i$ is the phase lag between the external load of the $i$th ray and the sway motion. $F_0$ is assumed to be uniform along each ray, and its exact value is selected via numerical tests; i.e., the desired deformation patterns are activated while maintaining the numerical stability. In the present work, $F_0$ is chosen to be $1.1\rho U_\infty^2 c^2$.

For such a caudal fin model, the deforming pattern is primarily determined by the exact distribution of $\varphi_i$, especially the mean phase ($\varphi_{\text{mean}}$) of the rays and the phase difference ($\varphi_{\text{diff}}$) between the maximum and minimum values of $\varphi_i$. In the present work, we examine four different phase distributions among the fin rays:

Distribution I:

$$\varphi_i = \varphi_{\text{mean}}, \quad \varphi_{\text{diff}} = 0$$

Distribution II:

$$\varphi_i = \varphi_{\text{mean}} + \varphi_{p,i} - \varphi_0 \tag{1}$$

where $\varphi_0 = 180$, and $\varphi_{p,i}$ is computed as

$$\varphi_{p,i} = \varphi_0 Q_i/Q \tag{2}$$

where

$$Q_i = 1 + \lambda\sin\left(\frac{\pi(i-1)}{N-1}\right)$$

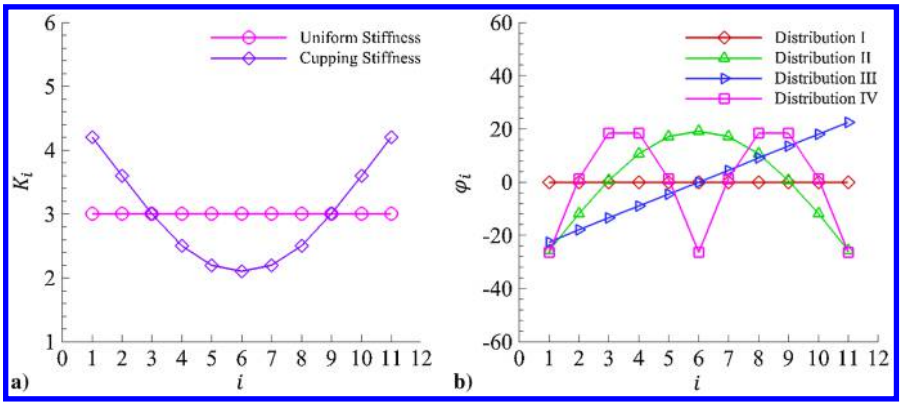


**Fig. 2 Representations of a) normalized bending stiffness of $i$th ray in uniform and cupping stiffness distributions ($K_b = 3.0$) and b) phase lag of $i$th ray in different distributions ($\varphi_{\text{mean}} = 0$ deg and $\varphi_{\text{diff}} = 45$ deg).**

and

$$Q = \frac{1}{N}\sum_{i=1}^{N} Q_i$$

The parameter $\lambda$ is determined by ensuring $\max\{\varphi_{p,i}\} - \min\{\varphi_{p,i}\}$ is equal to the designed value of $\varphi_{\text{diff}}$.

Distribution III:

$$\varphi_i = \varphi_{\text{mean}} + \frac{2i - N - 1}{2(N-1)}\varphi_{\text{diff}} \tag{3}$$

Distribution IV:

$$\varphi_i = \varphi_{\text{mean}} + \varphi_{p,i} - \varphi_0 \tag{4}$$

where $\varphi_0 = 180$, and $\varphi_{p,i}$ is computed as

$$\varphi_{p,i} = \varphi_0 Q_i / Q \tag{5}$$

where

$$Q_i = 1 + \lambda\left|\sin\left(\frac{2\pi(i-1)}{N-1}\right)\right|$$

and

$$Q = \frac{1}{N}\sum_{i=1}^{N} Q_i$$

The parameter $\lambda$ is determined by ensuring $\max\{\varphi_{p,i}\} - \min\{\varphi_{p,i}\}$ is equal to the designed value of $\varphi_{\text{diff}}$.

Different phase distributions are plotted in Fig. 2b. These distributions are determined to reproduce certain deformation patterns similar to a real fish's caudal fin. It is seen that, in distribution I, the phase lag is uniform among the rays. Distribution II has the maximum phase lag achieved at the ray in the middle (ray 6), whereas the rays at the dorsal and ventral edges have the minimum value. This phase distribution is expected to generate cup deformations. Distribution III is designed to achieve the *H* mode or *S* mode (which cannot be accomplished via purely passive deformations). Distribution IV has a W-shape phase distribution, where the rays at the dorsal and ventral edges have the same phase lag as the ray at the center. This type of phase distribution is used to activate W-shape deformations observed in live fishes.

The propulsion performance of the fin is characterized by the mean thrust coefficient $\overline{C}_T$, the mean vertical force coefficient $\overline{C}_Z$, the mean power expenditure coefficient $\overline{C}_P$, and the propulsion efficiency $\eta$. These mean values are evaluated by averaging the instantaneous coefficients over one motion period $T$. The instantaneous thrust coefficient is defined as

$$C_T(t) = \frac{-F_X(t)}{0.5\rho U_\infty^2 c^2} \tag{6}$$

where $F_X(t)$ is the $x$ component of the instantaneous hydrodynamic force $\boldsymbol{F}(t)$.

Similarly, we have

$$C_Y(t) = \frac{F_Y(t)}{0.5\rho U_\infty^2 c^2},$$
$$C_Z(t) = \frac{F_Z(t)}{0.5\rho U_\infty^2 c^2},$$
$$C_P(t) = \frac{P(t)}{0.5\rho U_\infty^3 c^2} \tag{7}$$

where $F_Y(t)$ and $F_Z(t)$ are the components of the instantaneous hydrodynamic force $\boldsymbol{F}(t)$ in the $y$ and $z$ directions, respectively; and $P(t)$ is the instantaneous power expenditure, which is evaluated as

$$P(t) = \iint_S -\boldsymbol{F}(\boldsymbol{x}, t)\cdot \boldsymbol{V}_g(\boldsymbol{x}, t)\,\mathrm{d}\boldsymbol{x} \tag{8}$$

where $\boldsymbol{V}_g(\boldsymbol{x}, t)$ is the moving velocity of the fin. It should be noted that the present definition of $P(t)$ measures the work done to the surrounding fluid by the caudal fin, which equals the power from the actuation forces (including the sway motion and the distributed external load) if it is assumed that there is no power loss during the mechanical transmission. We also assume that the energy transferred from the fluid to the caudal fin cannot be reused; thus, the negative values of $C_P(t)$ are set to be zero [15]. Therefore, the propulsion efficiency $\eta$ is calculated as

$$\eta = \frac{\overline{C}_T}{\overline{C}_P} \tag{9}$$

We would like to highlight that the present study is not meant to exactly duplicate the dynamics of the caudal fin of a certain fish species. Instead, we create an idealized fin model that resembles some particular features of a fish caudal fin in general. Although the present model captures the ray-supported characteristic of real fish fins, the geometry and mechanical properties are very different from those of any particular fish fin. Besides, the activation mechanism of real fish fins is more complicated than the one used in the present model. Therefore, it is not possible to quantitatively compare the present results to experimental observations. However, we do have some conclusions that are qualitatively similar to experimental study; e.g., the *S* mode is suitable for a braking maneuver, which will be explained in detail in Sec. IV.

## III. Mathematical Formulation and Numerical Methods

The key modules in the present fluid–structure interaction model are a fluid solver based on an overset, multiblock structured grid and a nonlinear beam model resolving the structural dynamics.

The fluid solver numerically solves the unsteady compressible Navier–Stokes equations, which is written in its integral form

$$\frac{\partial}{\partial t}\iiint_V \boldsymbol{U}\,\mathrm{d}V + \iint_{\partial V}\boldsymbol{G}\,\mathrm{d}\boldsymbol{S} - \iint_{\partial V}\boldsymbol{H}\,\mathrm{d}\boldsymbol{S} = 0 \tag{10}$$

where $\boldsymbol{U} = (\rho, \rho\boldsymbol{v}, \rho E)^T$ is the conservative variable vector, $V$ is the control volume, $\partial V$ is the boundary surface enclosing the volume, and $\boldsymbol{S}$ is the surface vector in the outward direction. Also, $\rho$ is the fluid density, $\boldsymbol{v}$ is the velocity vector, and $E$ is the total energy. $\boldsymbol{G}$ and $\boldsymbol{H}$ are the convective and diffusive flux vectors, respectively.

The fluid governing equations are discretized by a cell-centered finite volume method based on an overset multiblock structured grid system [13]. The convective flux is evaluated using the Jameson–Schmidt–Turkel scheme with artificial dissipation [16], whereas the derivatives of the velocity are estimated with Green's theorem. For time-dependent simulations, the dual-time-stepping algorithm [17] is employed for the temporal integration. At each time step, the domain connectivity is accomplished by an overset grid assembler based on an implicit hole-cutting technique [18].

It should be noted that the flow is assumed to be laminar in the present study. In relatively low-Reynolds-number regimes (below or on the order of $10^3$), the turbulence may play an insignificant role in the flowfield. For these scenarios, laminar flow models are usually used for biomimetic problems (see examples in Refs. [19–21]). The flow model is formulated with the compressible Navier–Stokes equations. To ensure that the compressibility is negligibly small, the freestream Mach number is chosen to be $M_{a,\infty} = 0.06$, which is far below the critical value for pronounced compressibility effect ($M_a = 0.3$) but still sufficiently large for

numerical stability. The Mach number used here is only a numerical parameter, and varying its value within a reasonable range will not have any significant effect on the results (see Sec. IV). Besides, the local Mach numbers in the complete computational domain are monitored to guarantee that they are below the critical value. The present compressible flow solver has been successfully applied to study different incompressible flow problems in previous work [13,22,23].

In the structural part, the dynamics of the nonlinear Euler–Bernoulli beam is governed by [24]

$$m_s \frac{\partial^2 \boldsymbol{x}}{\partial t^2} + K_b \frac{\partial^4 \boldsymbol{x}}{\partial s^4} - K_s \frac{\partial}{\partial s}\left\{\left[1 - \left(\frac{\partial \boldsymbol{x}}{\partial s}\frac{\partial \boldsymbol{x}}{\partial s}\right)^{-0.5}\right]\frac{\partial \boldsymbol{x}}{\partial s}\right\} = \boldsymbol{F}_f + \boldsymbol{F}_{sp} + \boldsymbol{F}_{ac} \tag{11}$$

where $\boldsymbol{x}$ is the instantaneous position of the ray, and $s(0 < s < c)$ is the Lagrangian coordinate. Also, $m_s = \rho_s h$ is the mass per unit length, where $\rho_s$ is the density of the fin rays. $K_b \equiv Eh^3/12$ and $K_s \equiv Eh$ represent the bending and stretching stiffnesses, respectively. On the right-hand side, $\boldsymbol{F}_f$ denotes the fluid load and $\boldsymbol{F}_{sp}$ represents the force exerted by the connecting linear springs that model the constraints from the collagenous membrane. $\boldsymbol{F}_{ac}$ is the distributed force along the beam, which models the pulling effect by the tendons at the basal end of the ray (see Fig. 1d). The hysteretic (or material) damping effect is considered by replacing the Young's modulus $E$ in $K_b$ and $K_s$ with $E(1 + \sigma\partial/\partial t)$, where $\sigma$ denotes the structural damping coefficient. In all present simulations, we select $\sigma = 2c/U_\infty$. Equation (11) is discretized using a second-order finite difference method, and the resulting linear system is solved with an iterative Gauss–Seidel method [24,25].

In the present algorithm, the Navier–Stokes solver is coupled with the nonlinear beam model via a partitioned framework. Compared with a strongly coupled algorithm, which requires iterations within each time step, a loosely coupled method needs only a single data exchange between the fluid solver and structural solver in each time step so that it significantly reduces the computational expense. Despite the numerical stability issue associated with loosely coupled methods [26], this approach is still favored due to its simplicity and efficiency. Since the caudal fin model is completely three-dimensional and requires plenty of computational time, a loosely coupled approach known as the conventional serial staggered procedure [27] is used in the present work. Due to the nonconformity between the fluid grid and the structural grid, interpolations of fluid forces and structural displacements must be performed at the fluid–structure interface. For the force interpolation, both the fluid grid nodes on the wet boundary of the body and the structural grid nodes are first projected to a common planar plane, on which a bilinear interpolation is then performed [13]. The structural displacements are transferred to the fluid mesh by a constant volume tetrahedron method [28,29].

## IV. Results

The ray-strengthened caudal fin problem depicted in Fig. 1 is solved using the fluid–structure interaction solver described in Sec. III. The computational domain and fluid mesh used in the present paper are the same as those in a previous publication by Shi et al. [13], and the Reynolds number based on the length of the ray is $Re = 1000$. The height of the first grid layer off the wall $\Delta y$ is calculated using a flat-plate boundary theory for a given $y+$ value. For the present Reynolds number, $y+$ is chosen to be 0.5, resulting in $\Delta y = 0.005c$. The present fluid–structure interaction solver has been validated via several canonical cases in a previous paper by Shi et al. [13]. The present fluid-structure interaction solver is further validated by predicting the dynamics of a three-dimensional flexible plate immersed in a uniform flow and comparing with experimental data [30]. The Reynolds number based on chord length $L$, incoming flow velocity $U_0$, and kinematic viscosity is 6000. The leading edge of the plate undergoes a harmonic heave motion of $y = a_0 \cos(2\pi f t)$, where $a_0 = 0.033L$ and $f$ is the heave frequency. The reduced frequency is defined as $f_r = \pi f L/U_0$. The dimensionless bending stiffness is $K_b = 4.2$ and the mass ratio is $\bar{m} = 0.3$ both are consistent with the experiment.

Figure 3a shows the results of a sensitivity study to mesh density and time step. It is seen that the result of mesh_M (medium density; $dt = T/120$) overlaps exactly with that of mesh_F (fine density; $dt = T/160$), indicating that convergence has been reached and the further increase of mesh density and decrease of time step will not significantly affect the numerical result. The effect of the freestream Mach number is demonstrated in Fig. 3b, which demonstrates the insensitivity of the result to the Mach number as long as it is sufficiently large for numerical stability. For the rest of the simulations, the Mach number is fixed at 0.06.

Figures 4a and 4b illustrate the normalized trailing-edge amplitude and phase lag of the leading and trailing edges as functions of the reduced frequency. The present numerical results show good agreement with the experimental data [30]. Similar deformation patterns are also obtained, as demonstrated in Fig. 4c.

In the present paper, we carry out an additional self-consistency study to justify the fluid mesh, physical time step, and number of nodes along the beam we use here. To check the sensitivity to the fluid mesh, three meshes with different densities are generated, which are termed as mesh_F (fine mesh, with 5 million grid cells), mesh_M (medium mesh, with 3.7 million grid cells), and mesh_C (coarse mesh, with 2.8 million grid cells). These meshes have the same sizes as those used in a previous paper by Shi et al. [13]. Similarly, three physical time steps ($dt = T/160, T/200$, and $T/240$) and three numbers of grids along each ray ($N_{bm} = 81, 101$, and 121) are chosen for this sensitivity study. Figures 5a–5c demonstrate the sensitivity of the present code to the fluid mesh density, time-step size, and number of points along the beam. The time-averaged thrust coefficients and the errors relative to the result from mesh_F with $dt = T/200$ and $N_{bm} = 121$ are summarized in Table 1. It is seen that with sufficiently high fluid/structural mesh densities and a sufficiently small time step, the results are not sensitive to numerical parameters. Based on the

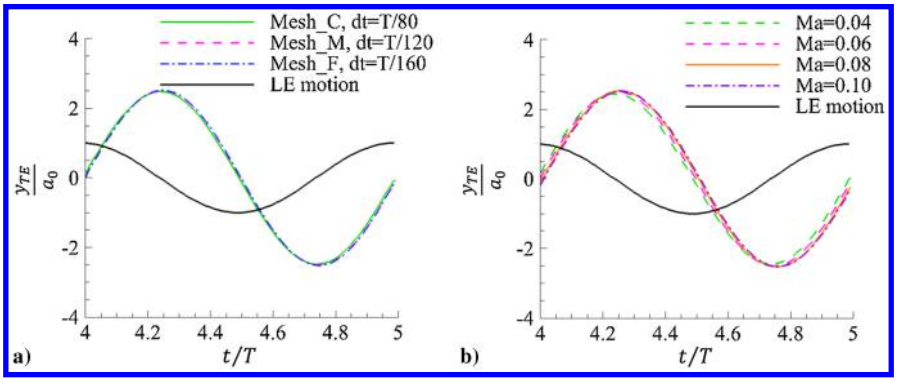


**Fig. 3 Numerical sensitivity with respect to a) mesh density and time step at $M_a = 0.06$, and b) effect of freestream Mach number at mesh_M ($dt = T/120$). Curves illustrate leading-edge (LE) and trailing-edge (TE) displacements of plate at $f_r = 5.6$.**

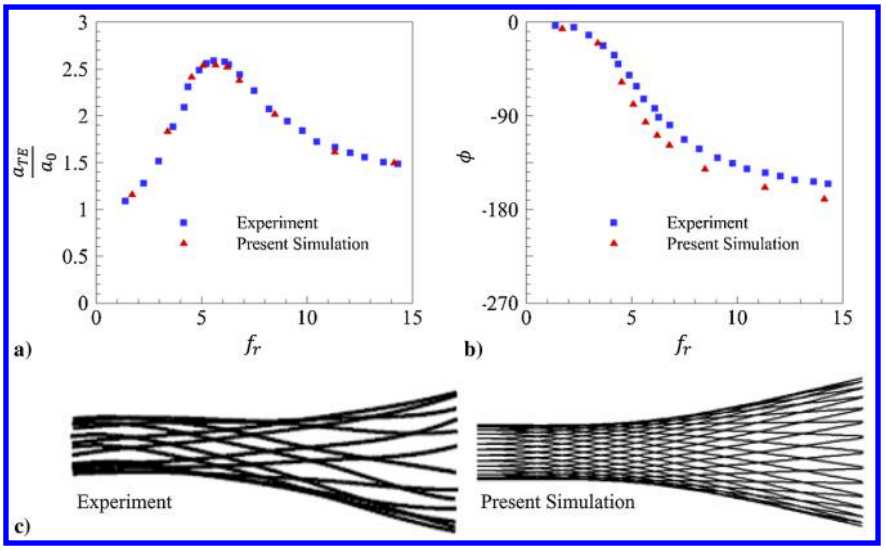


**Fig. 4 Representations of a) dimensionless trailing-edge amplitude as function of reduced frequency, b) phase lag (in degrees) between the LE and TE motions as function of reduced frequency, and c) deformation patterns of midline of plate.**

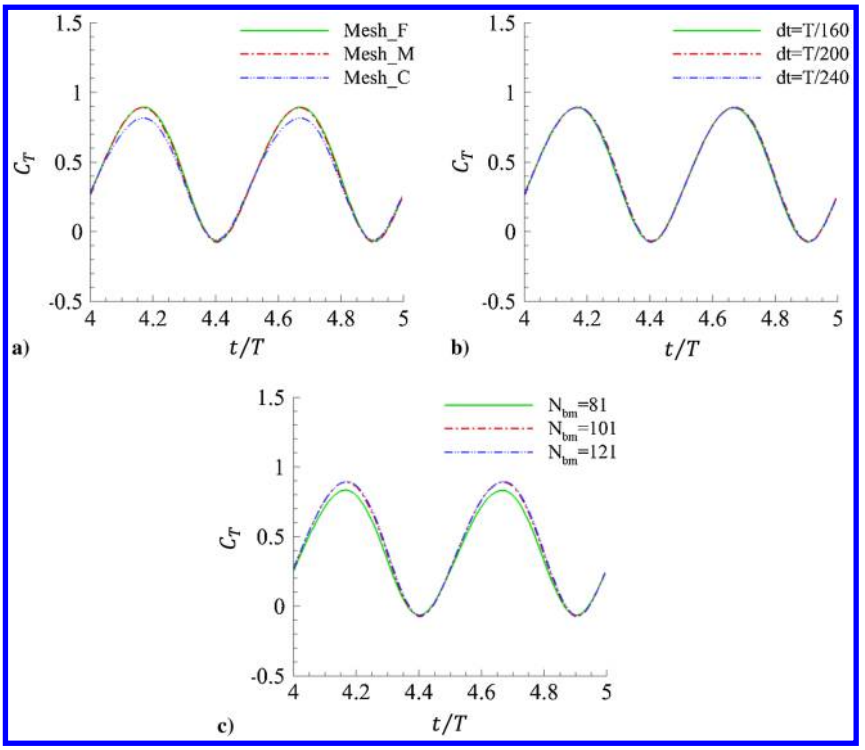


**Fig. 5 Sensitivity study of present code to a) computational fluid dynamics mesh density, b) time-step size, and c) number of nodes along beam. Fin has cupping stiffness distribution II with $\varphi_{\text{diff}} = 45$ deg and $\varphi_{\text{mean}} = 30$ deg.**

**Table 1 Summary of the self-consistency study results (see Fig. 5 for physical parameters)**

| | $dt$ | $N_{bm}$ | $\bar{C}_T$ | Error, % |
|---|---|---|---|---|
| Mesh_F | $T/200$ | 101 | 0.443 | 0.0 |
| Mesh_M | $T/200$ | 101 | 0.437 | −1.4 |
| Mesh_C | $T/200$ | 101 | 0.412 | −7.0 |
| Mesh_M | $T/160$ | 101 | 0.436 | −1.6 |
| Mesh_M | $T/240$ | 101 | 0.438 | −1.1 |
| Mesh_M | $T/200$ | 81 | 0.405 | −8.6 |
| Mesh_M | $T/200$ | 121 | 0.439 | −0.9 |

self-consistency study, the following simulations are based on mesh_M, $dt = T/200$, and $N_{bm} = 101$.

### A. Fin Deformation

The typical deformation patterns of the caudal fin in the present study are demonstrated in Fig. 6. The notation "U-I-0" stands for uniform stiffness, phase distribution I, and $\varphi_{\text{diff}} = 0$. Similarly, "C-II-45" means cupping stiffness, phase distribution II, and $\varphi_{\text{diff}} = 45$ deg. Other notations are defined in a similar way. As concluded in previous work by Shi et al. [13], the passively deformed fin with uniform stiffness (Fig. 6a) leads to a *C* mode (in which the dorsal and ventral edges lead the sway motion, whereas the central part falls behind) due to the nonuniformly distributed fluid force. Similar *C* mode patterns are also

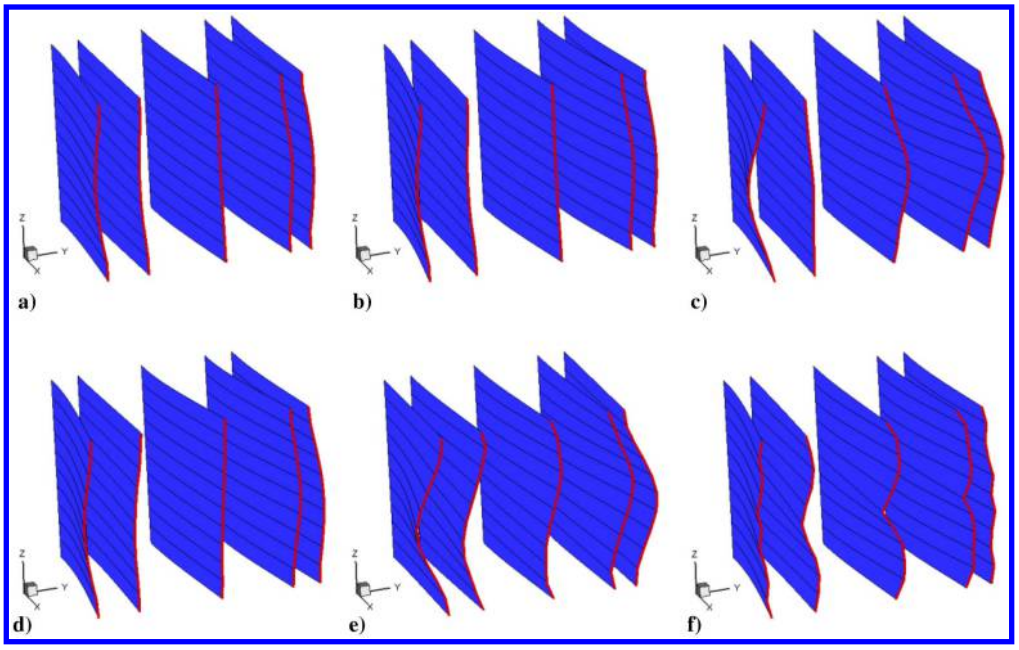


**Fig. 6 Fin deformations within half-motion period. Fin moves in negative-$y$ direction at positions $t = 0, T/8, T/4$, and $T/2$: a) U-passive, b) U-I-0, c) C-II-45, d) U-III-90, e) U-III-360, and f) U-IV-90. For all cases, $\varphi_{\text{mean}} = 30$ deg.**



achieved by the fin with distribution U-I (Fig. 6b). With distribution C-II, the caudal fin displays a more significant cupping pattern (Fig. 6c) at a small phase difference ($\varphi_{\text{diff}} = 45$).

For distribution U-III, the fin exhibits an asymmetrical deformation pattern. As the phase difference increases, the fin's deformation gradually transforms from the $H$ mode, which is shown in Fig. 6d, to the $S$ mode, which is illustrated in Fig. 6e. Compared with the $H$ mode, the $S$ mode shows a wavelike deformation pattern, which is not possible to be accomplished by purely passive deformation. This mode is observed in experiments [9] to be associated with the braking maneuver. Incidentally, we find that the $S$ mode generates less thrust and lateral force in comparison with the $H$ mode, but it still creates vertical force that may be needed for motion stabilization, which makes the $S$ mode ideal for the braking process. With distribution U-IV, the $W$ mode is observed as demonstrated in Fig. 6f. For distribution U-IV, the rays at the dorsal, ventral edges and the center of the fin have the same phase lag in terms of the activation force with respect to the sway motion.

Figure 7 illustrates the actual deflections of ray 1 and ray 6 for the U-passive case (Fig. 7a) and the C-II-45 case at $\varphi_{\text{mean}} = 30$ (Fig. 7b). For both cases, the rays exhibit only a first-order bending mode and ray 6 has a larger lateral excursion than ray 1. Compared with the passive case, ray 6 of C-II-45 (with active control) creates significantly larger deformation. Considering that the profiles along ray 6 for both passive and active cases are very similar to each other (see Figs. 20c and 20d). A larger lateral deformation could lead to a better oriented total force, and thus result in higher thrust for the C-II-45 case.

### B. Force Generation and Propulsion Efficiency

Figure 8 shows the instantaneous thrust and power expenditure coefficients within one motion period. The fin with distribution U-II-45 generates significantly higher thrust peaks than the corresponding passive case with a slight increase in power expenditure (see Figs. 8a and 8b). With cupping stiffness distribution, the thrust of the C-II-45 case can be further enhanced while consuming very similar input power to the U-II-45 case.

The time-averaged thrust coefficient and propulsion efficiency of various stiffness and phase distributions are summarized in Figs. 9 and 10. For all types of phase distributions and most phase difference values, $\overline{C}_T$ and $\eta$ have similar variation trends as functions of $\varphi_{\text{mean}}$. Specifically, $\overline{C}_T$ decreases monotonously as the increase of $\varphi_{\text{mean}}$, whereas the propulsion efficiency, on the other hand, rises slightly and then declines with the increase of $\varphi_{\text{mean}}$. Besides, for all cases with active control, the thrust and propulsion efficiency of the fin are significantly enhanced when $\varphi_{\text{mean}}$ is less than 90 deg. For example, the thrust and propulsion efficiency of the fin with distribution U-II-45 are improved by 43% ($\varphi_{\text{mean}} = 0$) and 35% ($\varphi_{\text{mean}} = 60$), respectively. In terms of thrust generation and propulsion efficiency, smaller phase difference values produce better performance. This is reminiscent of the experiment of Esposito et al. [10], where the cupping motion was created by imposing phase lags of 25 and 50 deg between the middle fin rays and the dorsal and ventral fin rays. Besides, in their experiment, cupping motion generated the largest thrust force compared with other motions.

Figures 11a and 11b compare the time-averaged thrust coefficient and propulsion efficiency between different stiffness and phase distributions at a fixed value of $\varphi_{\text{diff}}$ (hereby $\varphi_{\text{diff}} = 45$, except for distribution U-I, where $\varphi_{\text{diff}} = 0$). With uniform stiffness, for the parameters considered in the present study, the propulsion performances of the fin at different phase distributions are quite similar to each other, although they are significantly higher than the one with passive deformation only when $\varphi_{\text{mean}}$ is less than 90 deg. With distribution C-II, the fin's propulsion performance is significantly augmented.

Figure 11c demonstrates the vertical force coefficients for distribution U-III at different values of the phase difference. For all phase difference values, two maximum vertical forces are generated at $\varphi_{\text{mean}} = 0$ (in $-z$ direction) and $\varphi_{\text{mean}} = 120$ (in $+z$ direction). It suggests that a fish can control the phase distribution among the rays of its caudal fin to change both the magnitude and direction of the vertical force, which may play a significant role in body stabilization. This vertical force can provide the lift needed to counteract the gravity and create a torque around the center of mass of the fish to balance the torque (with opposite sign) generated by the pectoral fin.

During the braking process, the motion of the posterior part of the fish may be reduced in order to reduce the thrust generation. However, the vertical force may still be needed for stabilization. To elucidate this, we simulate cases with no sway motion at the leading edge of the fin. The fin with distribution U-III undergoes an $H$ mode at $\varphi_{\text{diff}} = 90$, whereas it undergoes an $S$ mode at $\varphi_{\text{diff}} = 360$ (see Figs. 6d and 6e). Figures 12a–12c illustrate the time-averaged values of the thrust, vertical force, and power expenditure coefficients. Without sway motion, the fin generates no thrust in both the $H$ mode and $S$ mode. However, the $S$ mode creates vertical force twice as much as the $H$ mode using similar input power. This is accompanied

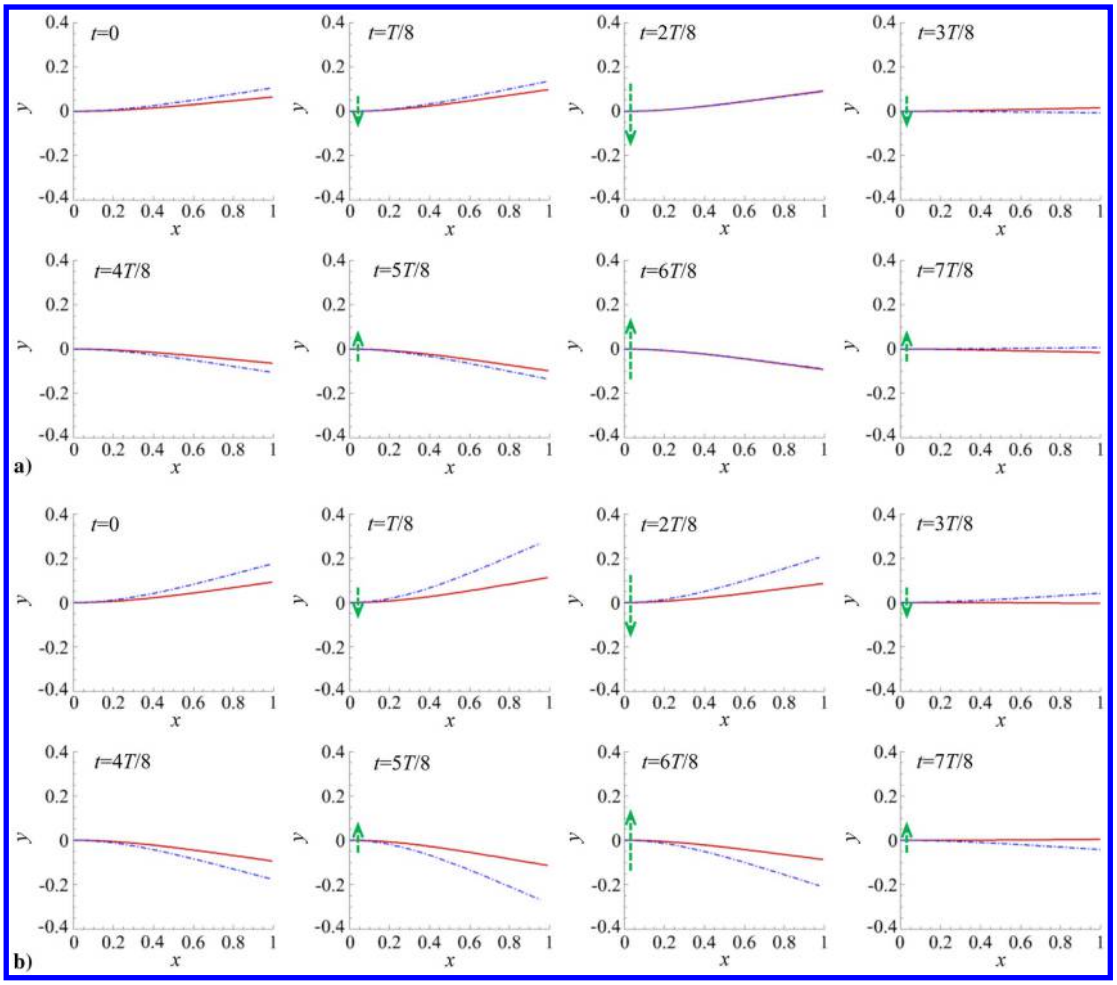


**Fig. 7 Deflections in *y* direction of ray 1 (red solid lines) and ray 6 (blue dashed–dotted lines) for a) U-passive, and b) C-II-45, with $\varphi_{\text{mean}} = 30$ deg.**

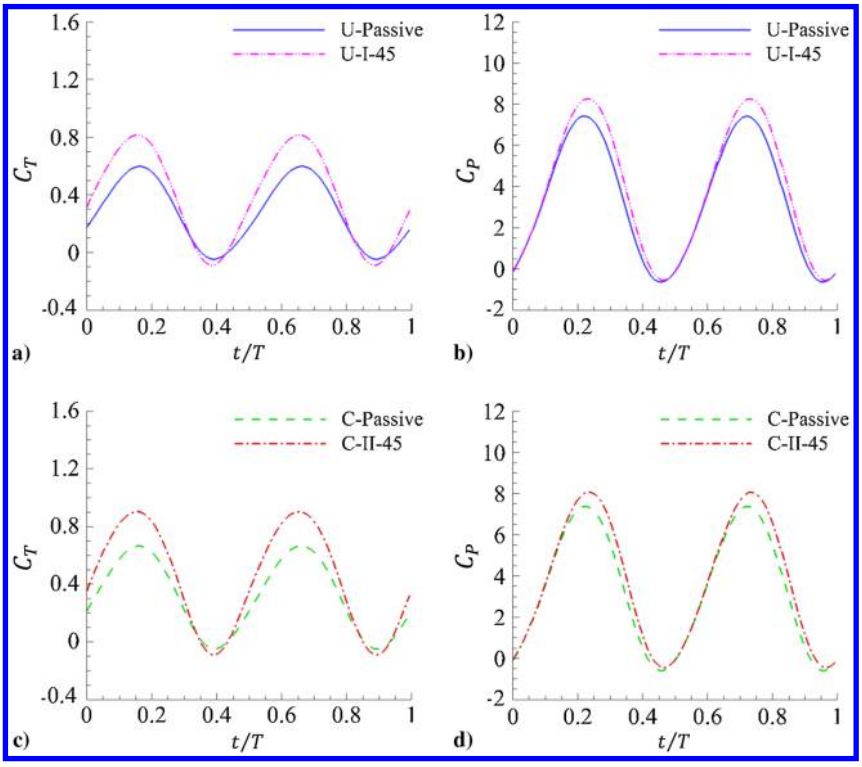


**Fig. 8 Time histories of $C_T$ and $C_P$ at various stiffness and phase distributions: $\varphi_{\text{mean}} = 30$ deg.**

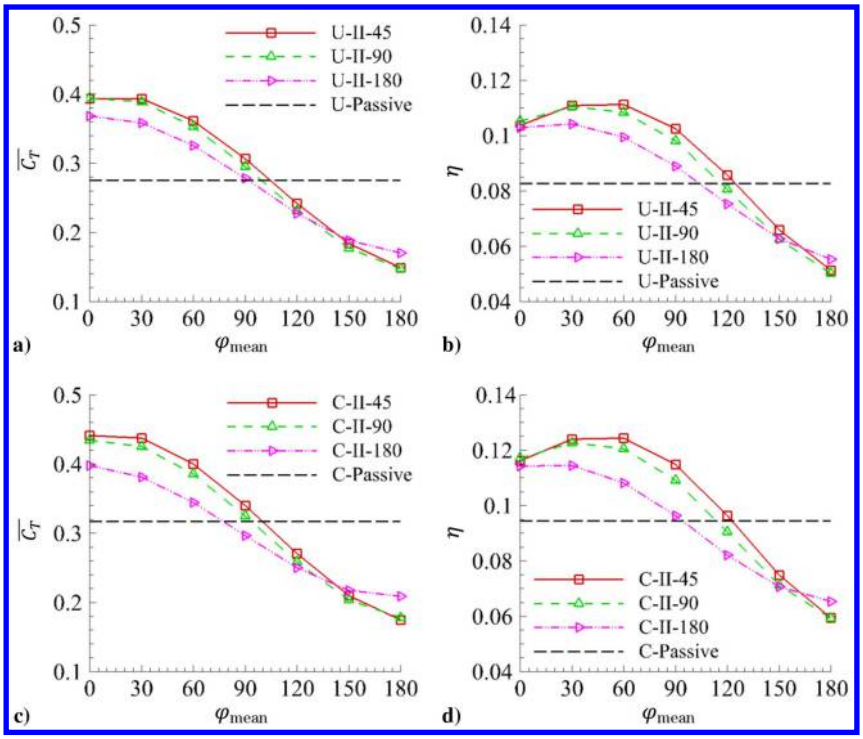


**Fig. 9 Time-averaged $C_T$ and $\eta$ as functions of mean phase lag $\varphi_{\mathrm{mean}}$ for a–b) U-II and c–d) C-II.**

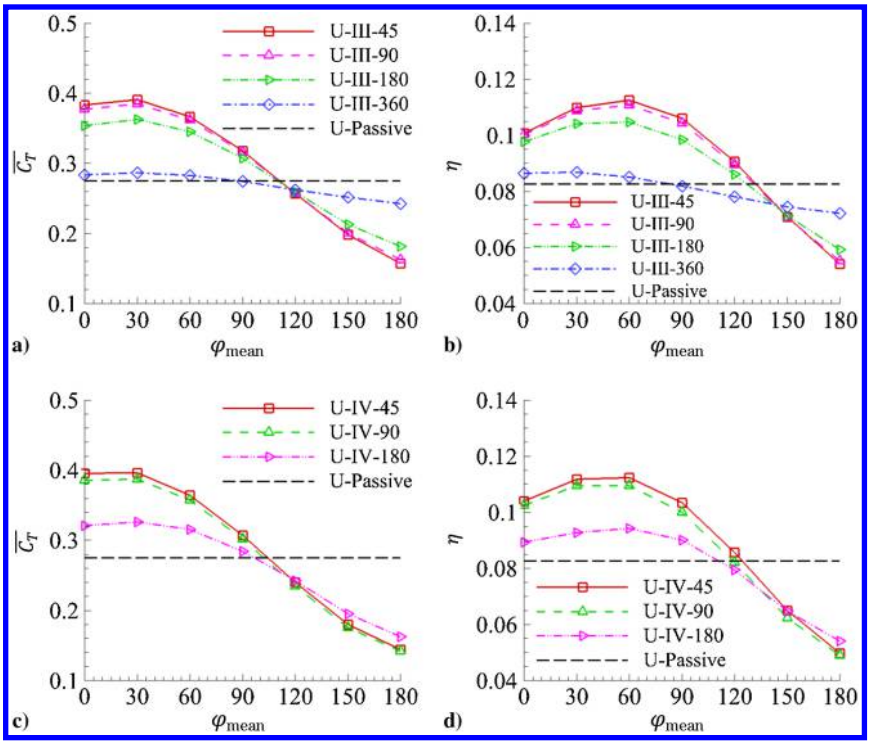


**Fig. 10 Time-averaged $C_T$ and $\eta$ as functions of mean phase lag $\varphi_{\mathrm{mean}}$ for a–b) U-III and c–d) U-IV.**

by significant reduction in lateral force in the *S* mode, as demonstrated in Fig. 12d. Therefore, we conclude that the *S* mode outperforms the *H* mode during the slowing down process. This is consistent with experimental observations.

### C. Near-Fin Flow Field

To further study the effect of active control over the caudal fin in sway motion and explain the physical underlying mechanisms in this fluid–structure interaction problem, we numerically visualize the near-fin flow field around the fin. Figure 13 shows the isosurfaces of vorticity magnitude in the wake behind the caudal fin for different deformation patterns. We can see that the wake is composed of a sequence of vortex rings, which are similar to those observed in previous studies [4]. These wake structures also resemble the hairpin structures proposed by Tytell [31] based on the particle image velocimetry study of the flow field around a bluegill sunfish. It is observed

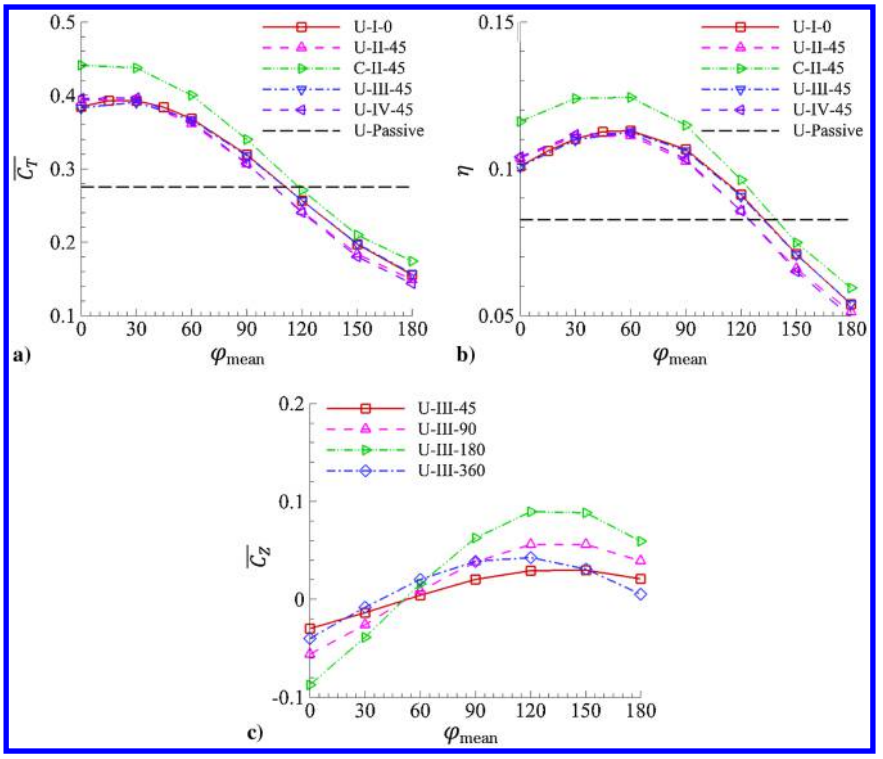


**Fig. 11 Time averaged a–b) $C_T$ and $\eta$ as functions of $\varphi_{\text{mean}}$ at various stiffness and phase distributions, and c) $C_Z$ as a function of $\varphi_{\text{mean}}$ for U-III.**

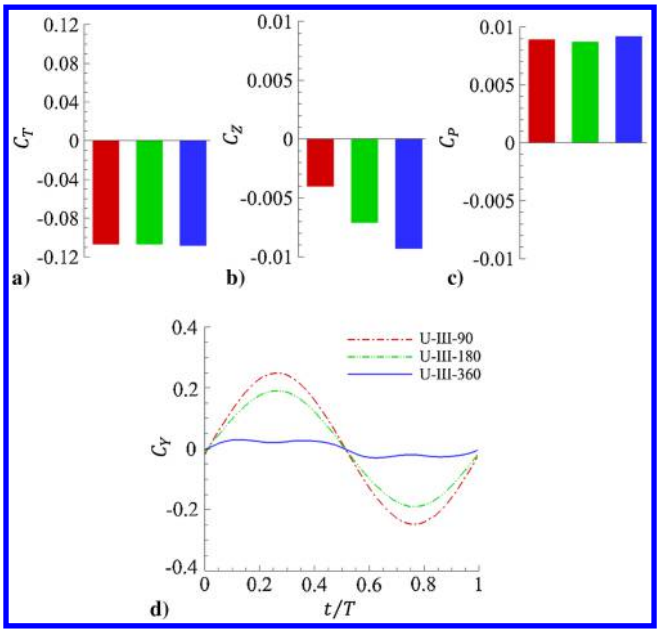


**Fig. 12 Time-averaged a) thrust, b) vertical force, and c) power expenditure coefficients of U-III without sway motion at $\varphi_{\text{diff}} = 90$ (red), 180 (green), and 360 (blue). Figure 12d shows time histories of $C_Y$ of U-III without sway motion.**

that, in the present study, the wake structures from different deformation patterns are qualitatively similar to each other.

Figure 14 demonstrates the sectional views of the flow vorticity within the $z$ plane and the $x$ plane. The vorticity of the U-passive case (Figs. 14a and 14c) and the C-II-45 case (Figs. 14b and 14d) in both the $x$ and $z$ planes are qualitatively similar. Specifically, in the plane $z = 0.5c$, we can observe the formations of a clockwise leading-edge vortex; and a counterclockwise vortex is shed at the trailing edge. It is not surprising that the vortex shedding patterns in Figs. 14a and 14b are similar to each other. As previously discussed, both the U-passive case and the C-II-45 case have only the first bending mode excited (see Fig. 7).

From the vorticity fields in plane $x = 0.7c$, we can see the formations of a clockwise vortex near the dorsal edge and a counterclockwise vortex near the ventral edge; and the vortices are symmetrical with respect to the midline (ray 6) due to the symmetrical deformation. The C-II-45 case has more pronounced spanwise cupping deformation so that the fluid at the central part has a tendency to flow toward the midline. This makes it difficult for the fluid to move around the dorsal and ventral edges, causing an increase of the pressure in the central region.

### D. Physical Mechanism for Performance Enhancement

The parametric exploration in Sec. IV.B indicates that the optimal performance occurs when $\varphi_{\text{diff}}$ is approximately 45 deg and $\varphi_{\text{mean}}$ is around 30 deg. To reveal the physical mechanism behind the performance improvement, the results will be further analyzed and discussed in this section.

The bending deformation shown in Fig. 7 essentially creates an effective yaw motion, as illustrated in Fig. 15. This yaw motion can be represented as $y_p = (y_T - y_L)/c$, where $y_L$ and $y_T$ are the lateral deflections of the ray's leading and trailing edges, respectively. It is observed in Fig. 15 that the yaw motion varies with time almost sinusoidally so that it can be approximated using a cosine function as $y_p(t) \sim A_p \cos(\omega_p t + \psi)$, where $A_p$ is the amplitude of the yaw motion and $\psi$ is the phase lag between the sway motion and the yaw motion.

Figure 16a demonstrates the yaw amplitudes of the rays at different stiffness and phase distributions. For uniform stiffness distribution, all the rays of U-II-45 have larger yaw angles than the rays of the corresponding passive case. With a cupping stiffness distribution (C-II-45), the yaw motions of the rays in the center of the fin are further increased, whereas those of the rays near the dorsal and ventral edges are suppressed, leading to a deeper cupping deformation. This is believed to further enhance the thrust generation. The phase lags between the sway motion and the effective yaw motion of

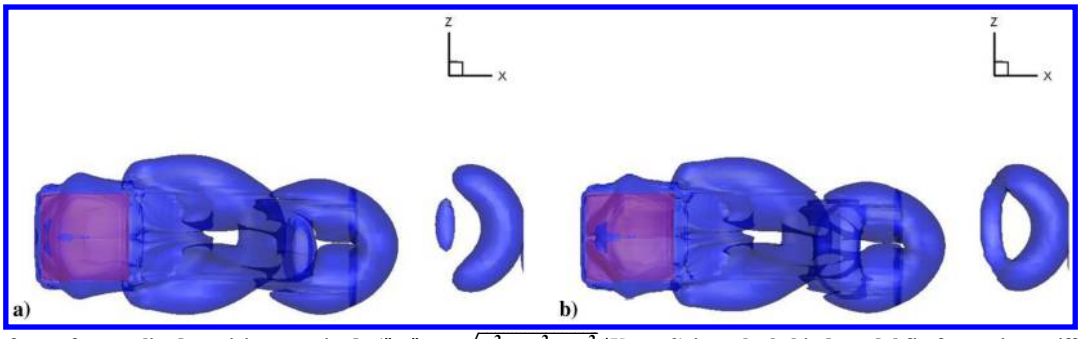


**Fig. 13 Isosurfaces of normalized vorticity magnitude ($\|\omega\| = c\sqrt{\omega_x^2 + y_x^2 + y_x^2}/U_\infty = 2$) in wake behind caudal fin for various stiffness and phase distributions at $t = 0.25T$: a) U-passive and b) C-II-45, with $\varphi_{\text{mean}} = 30$ deg.**



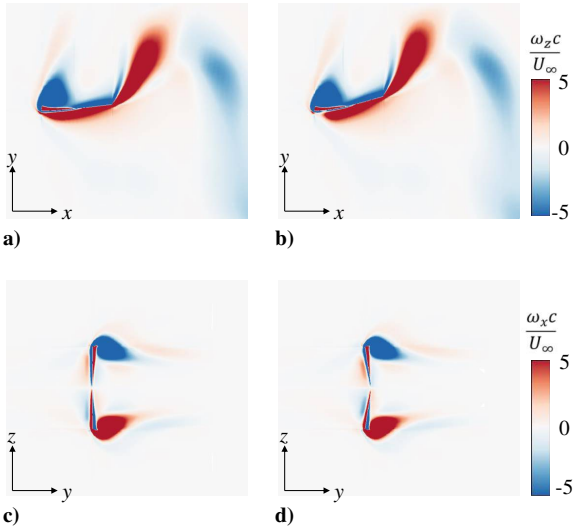


**Fig. 14 Vorticity fields for caudal fin of a and c) U-passive, and b and d) C-II-45, with $\varphi_{\text{mean}} = 30$ deg. Contours show normalized $z$ component of vorticity in plane $z = 0.5c$ (Figs. 14a–14b) and normalized $x$ component of vorticity in plane $x = 0.7c$ (Figs. 14c–14d) at $t = 0.25T$.**

the rays are shown in Fig. 16b. The averaged phase lags for all these three cases are actually close to each other (within the range of 35 to 45 deg). The implication is that, in these high-performance cases, the deformation caused by the active control mechanism and that due to passive structural flexibility are almost in phase with each other (see Fig. 16c); the primary mechanism of performance enhancement through active control is that it significantly increases the effective yaw amplitude (see Fig. 16a).

Incidentally, we note that by carefully choosing the structural flexibility of the rays, deformation and performance enhancement of actively controlled $C$-mode motion (e.g., the C-II 45 case) are in fact within reach using purely passive fin deformations [13]. The active control mechanism, however, greatly increase the versatility and adaptability of the system by making it easier to switch from one swimming mode to another to adjust for changes in the environment. Moreover, active control enables the $S$ mode, which is particularly useful in the braking maneuver (see Sec. IV.B).

To better understand the origin of thrust enhancement involved in the present study, the caudal fin surface is split into two parts: the dorsal–ventral part and the central part, as shown in Fig. 17. For the dorsal–ventral part (Fig. 17a), the force generated by the U-passive case has larger magnitude than those of the C-II-45 case, but the forces of the C-II-45 case are better oriented in the thrust direction. The advantage of active control is better illustrated in the central part (Fig. 17b), where the C-II-45 case has both larger force magnitude and better orientation.

As previously discussed, the cupping deformation tends to prevent the fluid from moving around the dorsal and ventral edges so that it may raise the pressure in the central area. This phenomenon can be more clearly observed in Figs. 18a and 18b, where the streamlines show the relative motion of the fluid with respect to the fin within plane $x = 0.7c$ at $t = T/4$. It is clearly seen that with the cup deformation, the streamlines near the central area of the fin (left-bottom part in Figs. 18a and 18b) remain horizontal very close to the surface of the fin, leading to a (slightly) wider high-pressure area. Figure 18c sketches three different spanwise deformation patterns, namely, flat, cup, and reverse cup. Intuitively, compared to flat deformation, the cup deformation may hold more fluid in the central region, thus leading to higher pressure in that region so that the resulting fluid dynamic force on the fin $F_{D2}$ should be larger than the other two cases. In contrast, the reverse cup deformation resembles a streamlined body (to certain extent), making it easier for the fluid to go around the upper and lower edges, thereby

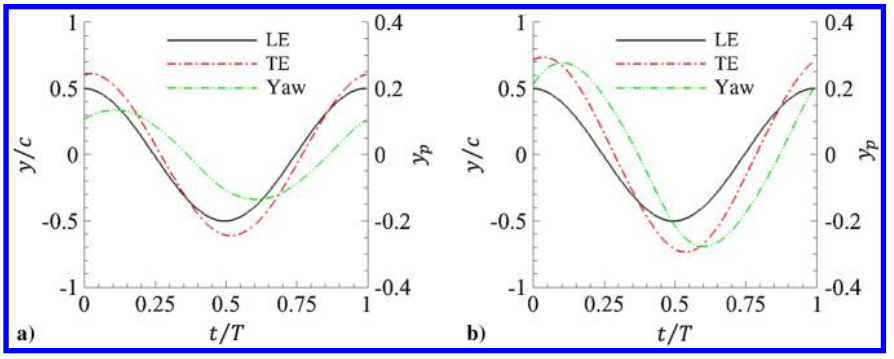


**Fig. 15 Time histories of normalized displacements of leading end $y_L/c$, trailing end $y_T/c$, and effective yaw motion $y_p = (y_T - y_L)/c$ of ray 6 at a) U-passive and b) C-II-45, with $\varphi_{\text{mean}} = 30$ deg.**

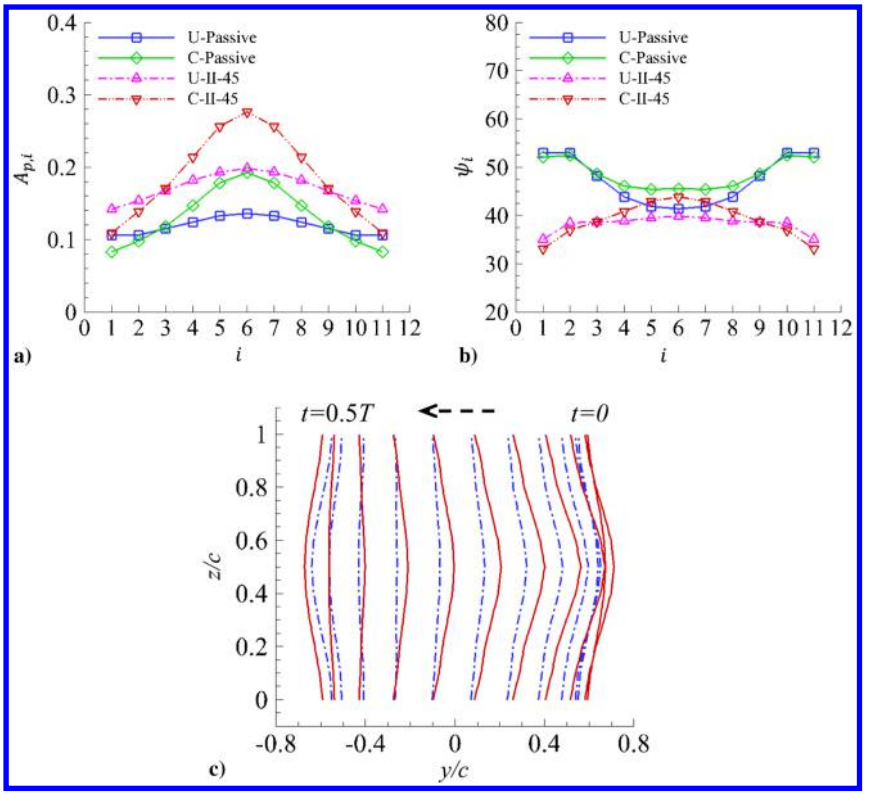


**Fig. 16 Representations of a) amplitudes ($A_{p,i}$) of effective yaw motions of rays, and b) actual phase lags ($\psi_i$). Figure 16c shows snapshots of trailing edge of fin for C-passive (blue dashed–dotted line) and C-II-45 (red solid line). Dashed arrow represents moving direction of leading edge, and $\varphi_{\text{mean}} = 30$ deg.**

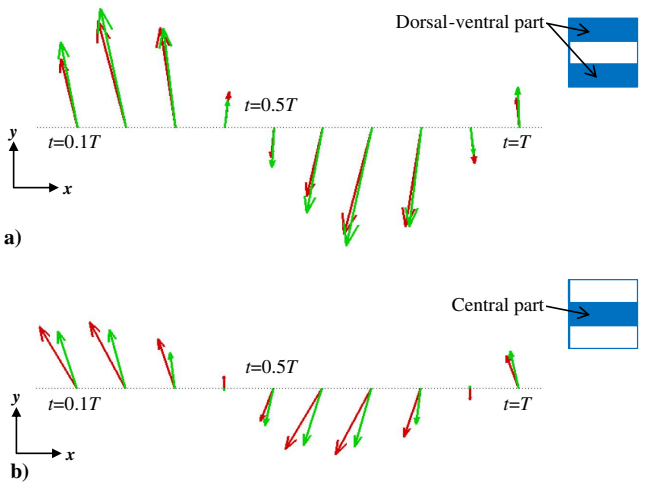


**Fig. 17 Force vectors of a) dorsal–ventral part and b) central part of fin within one motion period in $x$–$y$ plane: C-II-45 and $\varphi_{\text{mean}} = 30$ deg (red arrows) and U-passive (green arrows).**

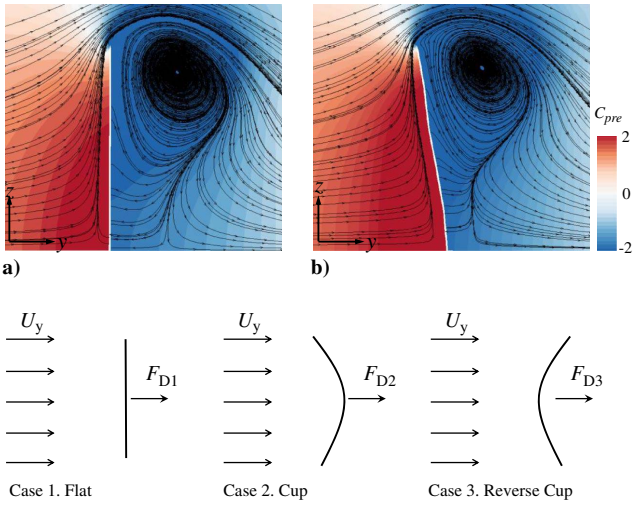


**Fig. 18 Pressure fields for caudal fins of a) U-passive and b) C-II-45, with $\varphi_{\text{mean}} = 30$ deg. Contours show pressure distribution in plane $x = 0.7c$ and $C_{\text{pre}} = (p - p_\infty)/0.5\rho U_\infty^2$. Figure 18c shows diagrams of three different spanwise deformations, where $U_y$ is flow speed relative to the fin.**

causing a decrease of pressure in the central area and a reduction in the force $F_{D3}$. Indeed, this kind of deformation has been shown to compromise the thrust generation [12].

Figures 19a–19d illustrate the pressure distributions over the fin surface for the U-passive case and the C-II-45 case. It is seen that in both cases, a high-pressure region exists within the areas of $0.4 < x/c < 0.8$ and $0.3 < z/c < 0.7$ at the negative-$y$ side of the fin. Compared with the U-passive case, the high-pressure region of the C-II-45 case is larger and stronger, whereas the pressure distributions on the positive side of the fin are very similar for the two cases. This explains why the C-II-45 case creates larger force in the central part of the fin (see Fig. 17). The pressure increase on the negative-y side can be quantitatively observed in Fig. 20a, where the pressure coefficients along the fin surface at $x = 0.7c$ are plotted. As the pressure distribution on the positive-y side is small, the increase of the pressure difference for the C-II-45 case (Fig. 20b) is mainly attributed to the stronger pressure region on the negative-y side of the fin.

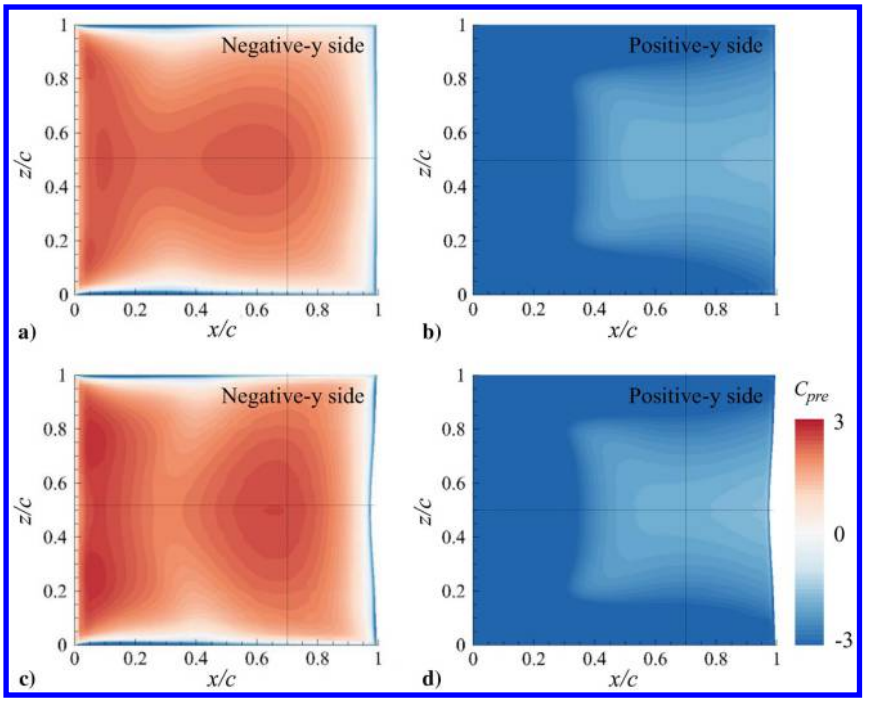


**Fig. 19 Pressure contours at two sides of caudal fin at $t = 0.25T$: a–b) U-passive and c–d) C-II-45, with $\varphi_{\text{mean}} = 30$ deg.**

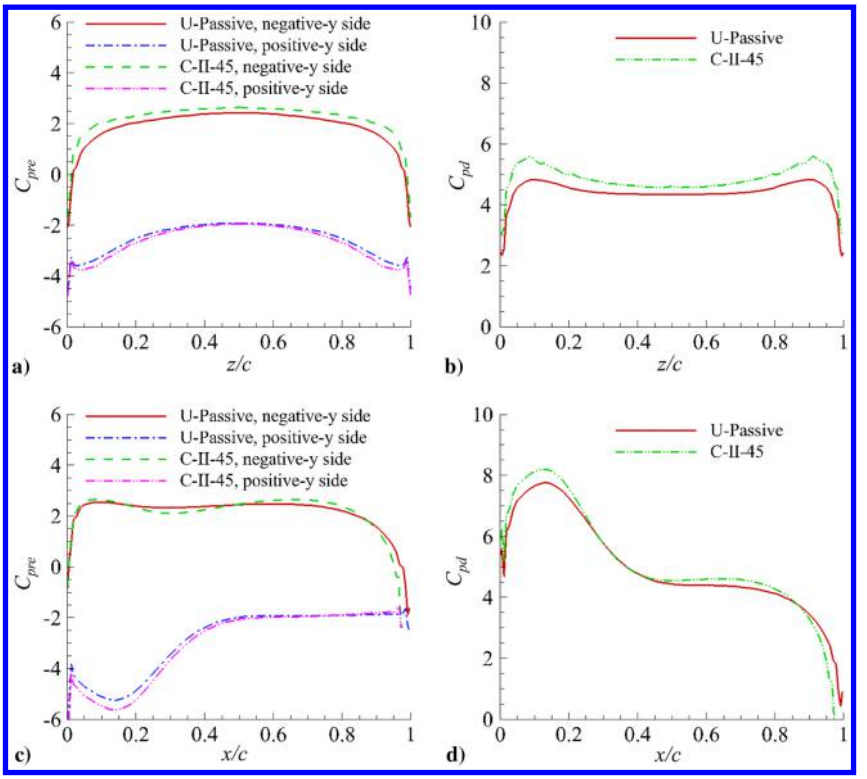


**Fig. 20 Pressure coefficients $C_{\text{pre}}$ along fin surface at a) $x = 0.7c$, and c) $z = 0.5c$. Pressure difference $C_{pd}$ between two sides of fin surface at b) $x = 0.7c$ and d) $z = 0.5c$.**

## V. Conclusions

Ray-finned fishes possess three distinctive features enabling the multi-degree-of-freedom control over the caudal fin: 1) anisotropic bending stiffness of the fin, 2) individual actuation of fin rays, and 3) ability of actively changing the flexibility and curvature of the rays. These unique characteristics have become an important source of inspiration for the design of artificial underwater robotics. Due to the complicated internal structures of fish fins, it is challenging to numerically model them. Some previous studies of ray-supported fins focused on features such as nonuniform flexibility and/or individual activation of the rays [4,12,13]. However, few studies have considered the active control on the curvature of the rays.

In the present paper, the performance of a simplified ray-strengthened caudal fin with both active and passive control strategies is numerically examined. In this model, the bony rays are represented by nonlinear Euler–Bernoulli beams, whereas the fluid dynamics is simulated by a Navier–Stokes solver. The caudal fin is activated

by 1) a sway motion shared by all the leading ends of the rays; and 2) time-varying external loads distributed uniformly along each ray, which mimic the pulling effect of the tendons at the basal end of each ray. The key parameters controlling the deformation of the fin are the maximum phase difference among the rays ($\varphi_{\text{diff}}$), the mean phase lag of the rays ($\varphi_{\text{mean}}$), and the phase distribution. By changing these parameters, different deformation patterns can be accomplished.

Four different phase distributions are investigated within the $\varphi_{\text{diff}} - \varphi_{\text{mean}}$ parameter space in the present study. Several deformation modes observed in previous experiments [9,10] are reproduced, including the *C* mode, the *W* mode, the *H* mode, and the *S* mode (which cannot be achieved with purely passive deformation). By comparing with the passive deformation case, it is found that the propulsion performances of all the cases with active control are significantly enhanced when $\varphi_{\text{mean}}$ is less than 90 deg. For example, the thrust force and propulsion efficiency of the U-II-45 case are improved by 43 and 35%, respectively.

Among these deformation patterns, the *C* mode created by the fin with distribution C-II-45 produces the best propulsion performance. This is attributed to two reasons. First, larger deflections and curvatures are created for the rays in the central part of the fin, which lead to higher yaw angles in the induced yaw motions. The forces are therefore better aligned in the thrust direction. Second, the chordwise bending and spanwise cupping deformations result in a larger, stronger, and further downstream high-pressure region, which further enhances the thrust generated by the *C* mode. In this particular mode, in terms of the performance enhancing mechanism, there is little difference between actively controlled and fully passive cases.

The *H* mode and *S* mode, on the other hand, both produce considerable vertical forces, which are primarily attributed to the asymmetrical deformations. Compared with the *H* mode, the *S* mode generates smaller thrust and vertical force while requiring less input power. This is reminiscent of the finding from a previous experiment [9] that the *S* motion is associated with the braking maneuver, during which the motion of the posterior part of the fish body may be reduced to decrease the thrust force. Thus, it is further demonstrated that without sway motion, the *S* mode actually generates much larger vertical force than the *H* mode. This, together with the significant reduction in lateral force, makes the *S* mode ideal during the braking process.

The present work is focused on demonstrating the effect of an active control strategy on the locomotion performance of a fishlike caudal fin instead of exactly duplicating a real fish fin. The present model captures several key characteristics possessed by real fins, e.g., anisotropic material property, individual ray activation, and active curvature control of the rays. However, it is also worth pointing out the limitations of the present study. For example, for simplicity, the present model is assumed to have a rectangular shape with rays of the same length. The aspect ratio of the current model is fixed at unity, whereas its effect is not examined. The present mass ratio is 0.2, which ensures the fin's deformation is fluid driven. But, its effect on the propulsion performance of the present caudal fin model is not studied either. Besides, the curvature changes of the rays are modeled as distributed external loads rather than explicitly modeling the bilaminar design of the real fin rays. For simplicity, the rotations at the basal ends of the rays are not considered either. The fins of a live fish have much more complicated internal structures, musculature, and nerve systems. It is thus difficult to directly relate the present results with the dynamics of actual fish fins. However, the conclusions from the present study may provide valuable inspirations and guidelines for the design of robotic fishes.

## Acknowledgments

The first author would like to thank the China Scholarship Council and the University of Strathclyde for the financial support during his study in the United Kingdom. Results were partially obtained using the ARCHIE-WeSt high-performance computer[§] based at the University of Strathclyde.

[§]Data available online at https://www.archie-west.ac.uk/ [retrieved 21 September 2020].

## References

[1] Triantafyllou, M. S., Techet, A. H., and Hover, F. S., "Review of Experimental Work in Biomimetic Foils," *IEEE Journal of Oceanic Engineering*, Vol. 29, No. 3, 2004, pp. 585–594. https://doi.org/10.1109/JOE.2004.833216

[2] Wen, L., and Lauder, G., "Understanding Undulatory Locomotion in Fishes Using an Inertia-Compensated Flapping Foil Robotic Device," *Bioinspiration and Biomimetics*, Vol. 8, No. 4, 2013, Paper 046013. https://doi.org/10.1088/1748-3182/8/4/046013

[3] Kancharala, A. K., and Philen, M. K., "Optimal Chordwise Stiffness Profiles of Self-Propelled Flapping Fins," *Bioinspiration and Biomimetics*, Vol. 11, No. 5, 2016, Paper 056016. https://doi.org/10.1088/1748-3190/11/5/056016

[4] Zhu, Q., and Shoele, K., "Propulsion Performance of a Skeleton-Strengthened Fin," *Journal of Experimental Biology*, Vol. 211, No. 13, 2008, pp. 2087–2100. https://doi.org/10.1242/jeb.016279

[5] Shoele, K., and Zhu, Q., "Fluid-Structure Interactions of Skeleton-Reinforced Fins: Performance Analysis of a Paired Fin in Lift-Based Propulsion," *Journal of Experimental Biology*, Vol. 212, No. 16, 2009, pp. 2679–2690. https://doi.org/10.1242/jeb.030023

[6] Shoele, K., and Zhu, Q., "Leading Edge Strengthening and the Propulsion Performance of Flexible Ray Fins," *Journal of Fluid Mechanics*, Vol. 693, Feb. 2012, pp. 402–432. https://doi.org/10.1017/jfm.2011.538

[7] Alben, S., Madden, P. G., and Lauder, G. V., "The Mechanics of Active Fin-Shape Control in Ray-Finned Fishes," *Journal of the Royal Society Interface*, Vol. 4, No. 13, 2007, pp. 243–256. https://doi.org/10.1098/rsif.2006.0181

[8] Lauder, G. V., Madden, P. G. A., Tangorra, J. L., Anderson, E., and Baker, T. V., "Bioinspiration from Fish for Smart Material Design and Function," *Smart Materials and Structures*, Vol. 20, No. 9, 2011, Paper 094014. https://doi.org/10.1088/0964-1726/20/9/094014

[9] Flammang, B. E., and Lauder, G. V., "Caudal Fin Shape Modulation and Control During Acceleration, Braking and Backing Maneuvers in Bluegill Sunfish, Lepomis Macrochirus," *Journal of Experimental Biology*, Vol. 212, No. 2, 2009, pp. 277–286. https://doi.org/10.1242/jeb.021360

[10] Esposito, C. J., Tangorra, J. L., Flammang, B. E., and Lauder, G. V., "A Robotic Fish Caudal Fin: Effects of Stiffness and Motor Program on Locomotor Performance," *Journal of Experimental Biology*, Vol. 215, No. 1, 2012, pp. 56–67. https://doi.org/10.1242/jeb.062711

[11] Lucas, K. N., Thornycroft, P. J. M., Gemmell, B. J., Colin, S. P., Costello, J. H., and Lauder, G. V., "Effects of Non-Uniform Stiffness on the Swimming Performance of a Passively- Flexing, Fish-Like Foil Model," *Bioinspiration and Biomimetics*, Vol. 10, No. 5, 2015, Paper 056019. https://doi.org/10.1088/1748-3190/10/5/056019

[12] Zhu, Q., and Bi, X., "Effects of Stiffness Distribution and Spanwise Deformation on the Dynamics of a Ray-Supported Caudal Fin," *Bioinspiration and Biomimetics*, Vol. 12, No. 2, 2017, Paper 026011. https://doi.org/10.1088/1748-3190/aa5d3f

[13] Shi, G., Xiao, Q., Zhu, Q., and Liao, W., "Fluid-Structure Interaction Modeling on a 3D Ray-Strengthened Caudal Fin," *Bioinspiration and Biomimetics*, Vol. 14, No. 3, 2019, Paper 036012. https://doi.org/10.1088/1748-3190/ab0fbe

[14] Tangorra, J. L., Davidson, S. N., Hunter, I. W., Madden, P. G. A., Lauder, G. V., Dong, H., Bozkurttas, M., and Mittal, R., "The Development of a Biologically Inspired Propulsor for Unmanned Underwater Vehicles," *IEEE Journal of Oceanic Engineering*, Vol. 32, No. 3, 2007, pp. 533–550. https://doi.org/10.1109/JOE.2007.903362

[15] Yin, B., and Luo, H., "Effect of Wing Inertia on Hovering Performance of Flexible Flapping Wings," *Physics of Fluids*, Vol. 22, No. 11, 2010, Paper 111902. https://doi.org/10.1063/1.3499739

[16] Jameson, A., Schmidt, W., and Turkel, E. L. I., "Numerical Solution of the Euler Equations by Finite Volume Methods Using Runge Kutta Time Stepping Schemes," *14th Fluid and Plasma Dynamics Conference*, AIAA Paper 1981-1259, 1981. https://doi.org/10.2514/6.1981-1259

[17] Jameson, A., "Time Dependent Calculations Using Multigrid, with Applications to Unsteady Flows Past Airfoils and Wings," *AIAA 10th Computational Fluid Dynamics Conference*, AIAA Paper 1991-1596, 1991. https://doi.org/10.2514/6.1991-1596

[18] Liao, W., Cai, J., and Tsai, H. M., "A Multigrid Overset Grid Flow Solver with Implicit Hole Cutting Method," *Computer Methods in Applied Mechanics and Engineering*, Vol. 196, Nos. 9–12, 2007, pp. 1701–1715. https://doi.org/10.1016/j.cma.2006.09.012

[19] Mittal, R., Dong, H., Bozkurttas, M., Lauder, G. V., and Madden, P., "Locomotion with Flexible Propulsors: II. Computational Modeling of Pectoral Fin Swimming in Sunfish," *Bioinspiration and Biomimetics*, Vol. 1, No. 4, 2006, Paper S35. https://doi.org/10.1088/1748-3182/1/4/S05

[20] Dong, H., Bozkurttas, M., Mittal, R., Madden, P., and Lauder, G. V., "Computational Modelling and Analysis of the Hydrodynamics of a Highly Deformable Fish Pectoral Fin," *Journal of Fluid Mechanics*, Vol. 645, Feb.2010, pp. 345–373. https://doi.org/10.1017/S0022112009992941

[21] Li, R., Xiao, Q., Liu, Y., Hu, J., Li, L., Li, G., Liu, H., Hu, K., and Wen, L., "A Multi-Body Dynamics Based Numerical Modelling Tool for Solving Aquatic Biomimetic Problems," *Bioinspiration and Biomimetics*, Vol. 13, No. 5, 2018, Paper 056001. https://doi.org/10.1088/1748-3190/aacd60

[22] Xiao, Q., and Liao, W., "Numerical Investigation of Angle of Attack Profile on Propulsion Performance of an Oscillating Foil," *Computers and Fluids*, Vol. 39, No. 8, 2010, pp. 1366–1380. https://doi.org/10.1016/j.compfluid.2010.04.006

[23] Liu, W., Xiao, Q., and Zhu, Q., "Passive Flexibility Effect on Oscillating Foil Energy Harvester," *AIAA Journal*, Vol. 54, No. 4, 2016, pp. 1172–1187. https://doi.org/10.2514/1.J054205

[24] Connell, B. S. H., and Yue, D. K. P., "Flapping Dynamics of a Flag in a Uniform Stream," *Journal of Fluid Mechanics*, Vol. 581, June 2007, pp. 33–67. https://doi.org/10.1017/S0022112007005307

[25] Zhu, Q., "Numerical Simulation of a Flapping Foil with Chordwise or Spanwise Flexibility," *AIAA Journal*, Vol. 45, No. 10, 2007, pp. 2448–2457. https://doi.org/10.2514/1.28565

[26] Causin, P., Gerbeau, J. F., and Nobile, F., "Added-Mass Effect in the Design of Partitioned Algorithms for Fluid-Structure Problems," *Computer Methods in Applied Mechanics and Engineering*, Vol. 194, Nos. 42–44, 2005, pp. 4506–4527. https://doi.org/10.1016/j.cma.2004.12.005

[27] Farhat, C., and Lesoinne, M., "Two Efficient Staggered Algorithms for the Serial and Parallel Solution of Three-Dimensional Nonlinear Transient Aeroelastic Problems," *Computer Methods in Applied Mechanics and Engineering*, Vol. 182, Nos. 3–4, 2000, pp. 499–515. https://doi.org/10.1016/S0045-7825(99)00206-6

[28] Goura, G. S. L., Badcock, K. J., Woodgate, M. A., and Richards, B. E., "A Data Exchange Method for Fluid-Structure Interaction Problems," *Aeronautical Journal*, Vol. 105, No. 1046, 2001, pp. 215–221. https://doi.org/10.1017/S0001924000025458

[29] Sadeghi, M., Liu, F., Lai, K. L., and Tsai, H. M., "Application of Three-Dimensional Interfaces for Data Transfer in Aeroelastic Computations," *22nd Applied Aerodynamics Conference and Exhibit*, AIAA Paper 2004-5376, 2004. https://doi.org/10.2514/6.2004-5376

[30] Paraz, F., Eloy, C., and Schouveiler, L., "Experimental Study of the Response of a Flexible Plate to a Harmonic Forcing in a Flow," *Comptes Rendus Mecanique*, Vol. 342, No. 9, 2014, pp. 532–538. https://doi.org/10.1016/j.crme.2014.06.004

[31] Tytell, E. D., "Median Fin Function in Bluegill Sunfish Lepomis Macrochirus: Streamwise Vortex Structure During Steady Swimming," *Journal of Experimental Biology*, Vol. 209, No. 8, 2006, pp. 1516–1534. https://doi.org/10.1242/jeb.02154

H. Dong
*Associate Editor*